nature photonics

ARTICLES

https://doi.org/10.1038/s41566-017-0070-7

Tandem luminescent solar concentrators based on engineered quantum dots

Kaifeng Wu[1,2], Hongbo Li[1,3] and Victor I. Klimov[1*]

Luminescent solar concentrators (LSCs) can serve as large-area sunlight collectors for terrestrial and space-based photovoltaics. Due to their high emission efficiencies and readily tunable emission and absorption spectra, colloidal quantum dots have emerged as a new and promising type of LSC fluorophore. Spectral tunability of the quantum dots also facilitates the realization of stacked multilayered LSCs, where enhanced performance is obtained through spectral splitting of incident sunlight, as in multijunction photovoltaics. Here, we demonstrate a large-area (>230 cm²) tandem LSC based on two types of nearly reabsorption-free quantum dots spectrally tuned for optimal solar-spectrum splitting. This prototype device exhibits a high optical quantum efficiency of 6.4% for sunlight illumination and solar-to-electrical power conversion efficiency of 3.1%. The efficiency gains due to the tandem architecture over single-layer devices quickly increase with increasing LSC size and can reach more than 100% in structures with window sizes of more than 2,500 cm².

Over the years, the reduction in the cost of solar electricity has been driven by advances in solar cell efficiencies as well as the reduced costs of materials, manufacturing and installation. An interesting opportunity to lower the price of solar energy further is through the use of inexpensive, large-area sunlight collectors based on a luminescent solar concentrator (LSC) technology[1–5]. An LSC comprises a slab of a transparent material containing highly emissive fluorophores (Fig. 1a)[1–3]. Solar photons incident on a larger-area device face (area A_1) are absorbed by the fluorophores, re-emitted at a longer wavelength, and waveguided by total internal reflection to the device edges (area A_2), where they are collected by photovoltaic (PV) cells. The ratio between A_1 and A_2 defines a geometric gain factor G, which is linked to the concentration factor C by $C=\eta_{s,ext}G$, where $\eta_{s,ext}$ is the external quantum efficiency (EQE) of the LSC, equal to the ratio of the edge-collected photon flux Φ_2 and the total incident solar flux $\Phi_{s,1}$ (Fig. 1a). The C factor can be thought of as an effective expansion coefficient of the active area of a solar cell, and if C is greater than unity then the use of an LSC can boost the photocurrent and thus the generated power. Moreover, if the per m² cost of an LSC is much lower than that of a PV module, then this scheme can allow for a reduction in the cost of solar electricity[6]. LSC technology can also enable new types of device such as semitransparent solar windows and solar sidings[4,7–10], lightweight optical antennas for space applications[11], and spectral reshapers for applications in photobiology and photochemistry[12].

Since being introduced in 1976[1], the LSC concept has been actively explored, with a primary focus on dye molecules[2–5,13]. Ordinary dyes, however, suffer from limited spectral coverage of the solar spectrum, low photoluminescence (PL) efficiencies at the near-infrared (NIR) wavelengths most suitable for coupling to Si PVs, and strong losses to reabsorption. The latter problem can be alleviated using approaches such as triplet emission or cascaded energy transfer, which can help spectrally displace the PL versus absorption spectrum[3,14,15].

Interesting new classes of LSC emitters introduced recently include the highly emissive perovskites[16,17], nanocluster phosphors[8] and colloidal nanocrystal quantum dots (QDs). Colloidal nanocrystals offer an unparalleled level of tunability of their absorption and emission spectra, combined with high photostability[6] and high PL quantum yields (η_{PL}) across the visible and NIR wavelengths[7,18–26]. Importantly, the major efficiency loss mechanism associated with self-absorption can be effectively tackled by a variety of strategies (commonly referred to as Stokes-shift engineering), including specially designed heterostructured QDs[6,21,23,24,26,27], impurity-doped structures[22,25], indirect-bandgap QDs[28], QDs emitting via intragap native defects[7,20,29] and hybrid QD–dye systems[30].

QDs with varied bandgaps are also well suited for the realization of multilayered LSCs, where each layer is designed so as to absorb a different part of the solar spectrum (Fig. 1a). As in the case of spectral splitting in multijunction solar cells[31–33], this approach can lead to a considerable boost in efficiency compared to single-layer devices[3,34,35]. The greatest benefit from this concept can be obtained by coupling each LSC layer to a bandgap-matched PV (Fig. 1a, left). However, as we show in this work, a considerable boost in the efficiency can be obtained even with the same type of PV (Fig. 1a, right) if the top, higher-energy-absorbing layer has a higher internal quantum efficiency ($\eta_{int}=\Phi_2/\Phi_{s,abs}$, where $\Phi_{s,abs}$ is the absorbed solar flux) than the bottom layer (Supplementary Notes 1 and 2).

Here, we report large-area, high-efficiency tandem QD LSCs fabricated using two types of QD, one with absorption onset in the NIR and the other in the visible. For the bottom layer, we use narrow bandgap $CuInSe_2$ (CISe)-based QDs that exhibit strong absorptance across the solar spectrum ($\eta_{s,abs}=\Phi_{s,abs}/\Phi_{s,1}$ up to ~30%) and a high η_{PL} of 65–75%. The top LSC layer is based on highly emissive Mn^{2+}-doped $Cd_xZn_{1-x}S$-based QDs ($\eta_{PL}=78\%$) with absorption onset at ~440 nm. Due to efficient excitation transfer from the semiconductor host to the emissive Mn^{2+} ions, PL in these structures occurs in a reabsorption-free intragap region, which results in an extremely high η_{int} of >50%. As a result, the high-energy portion of the solar

[1]Centre for Advanced Solar Photophysics, Los Alamos National Laboratory, Los Alamos, NM, USA. Present addresses: [2]State Key Laboratory of Molecular Reaction Dynamics and Collaborative Innovation Center of Chemistry for Energy Materials, Dalian Institute of Chemical Physics, Chinese Academy of Sciences, Dalian, China. [3]School of Materials Science and Engineering, Beijing Institute of Technology, Beijing, China. Kaifeng Wu and Hongbo Li contributed equally to this work. *e-mail: klimov@lanl.gov

© 2018 Macmillan Publishers Limited, part of Springer Nature. All rights reserved.

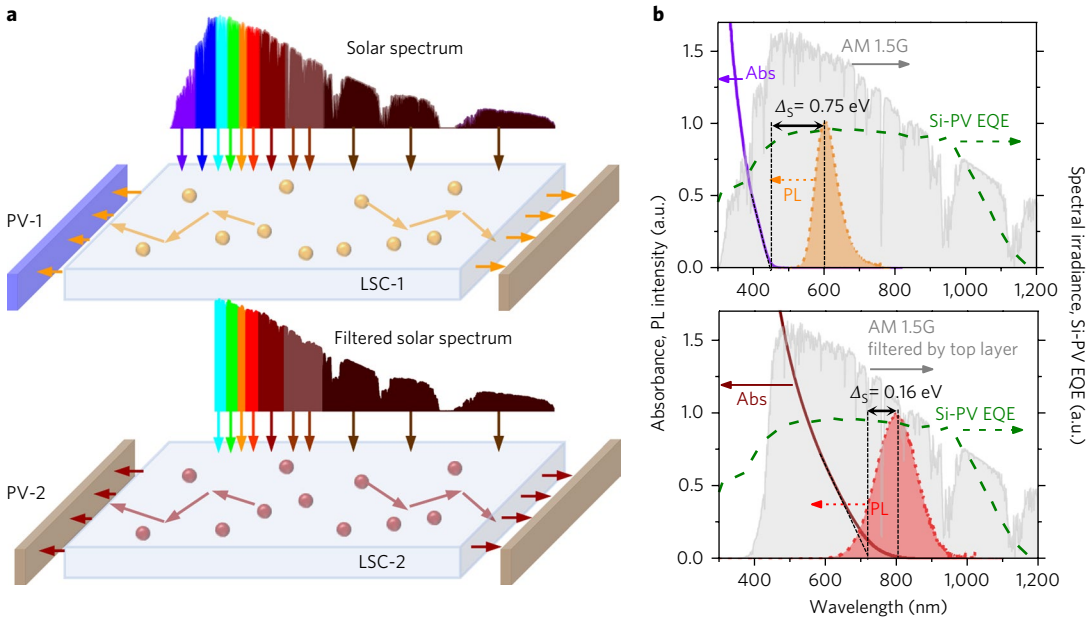

Fig. 1 | Concept of solar-spectrum splitting in a tandem LSC. a, A short-wavelength portion of the solar spectrum is absorbed by LSC's first layer (LSC-1), and the re-emitted light (orange arrows) is guided towards edge-mounted PVs. The longer-wavelength portion of the solar spectrum transmitted through LSC-1 is collected by LSC-2, which is equipped with its own set of PVs. For the best performance, this scheme should utilize bandgap-matched solar cells (PV-1 and PV-2, left). However, as discussed in the text, the overall LSC performance can be enhanced even with the same type of PVs used for both layers (right). **b**, Absorption (purple) and PL (orange) spectra of Mn^{2+}-doped $Cd_xZn_{1-x}S$/ZnS QDs used in LSC-1 along with the AM 1.5G solar spectrum (grey shading) and a typical Si PV EQE spectrum (green dashed line); top. The absorption (brown) and PL (red) spectra of $CuInSe_2$/ZnS QDs used in LSC-2 along with the AM 1.5G spectrum filtered by LSC-1; bottom.

spectrum harvested by the top layer is converted into the output flux much more efficiently than in the bottom layer, which results in the ~21% improvement in $\eta_{s,ext}$ and thus enhanced solar-to-electrical power conversion efficiency (PCE), even with the same type of PVs in both layers. The large-area tandem LSC (15.24 × 15.24 cm^2) coupled to GaAs solar cells exhibits a PCE of 3.1%, which can in principle be further enhanced to 3.8% using bandgap-matched PVs. This represents a 52% improvement versus a single bottom-layer device.

Bottom LSC layer

$CuInSe_xS_{2-x}$ (CISeS) QDs are well suited for use as the bottom layer of a tandem LSC. Due to their narrow bandgap (E_g = 1.02 eV for bulk CISe), these QDs allow for improved harvesting of the solar spectrum compared to wider-gap II–VI nanostructures. An additional advantage is a large intrinsic Stokes shift (Δ_S) between the PL band and the onset of strong absorption, which reflects the peculiarity of the emission mechanism in CISeS QDs. Due to a large abundance of native defects, the PL in these materials occurs not via a band-to-band transition but instead involves a transition between a conduction-band electron and a localized hole residing in an intragap state commonly ascribed to a Cu-related defect (denoted Cu* in Fig. 2a)[7,36] or a 'self-trapped' exciton[37]. As a result, the PL is situated at intragap energies, which greatly reduces its overlap with the absorption spectrum. In addition to its favourable spectral characteristics, the CISeS-QD PL is characterized by high η_{PL} (>50%) even at NIR wavelengths (>800 nm)[7], where common dyes are usually poor emitters (η_{PL} < 10%)[38].

As a result of the above properties, CISeS QDs have shown strong performance as LSC fluorophores. For example, the 12 × 12 cm^2 CISeS-QD-based devices of ref. [7] demonstrated an optical power efficiency ($\eta_{s,p}$) of 3.2%, which corresponded to an EQE of 3.7%; the two efficiencies are connected by $\eta_{s,p} = (\nu_{LSC}/\nu_s)\eta_{s,ext}$, where ν_s and ν_{LSC} are the average frequencies of the solar and LSC photons, respectively. These high efficiencies were obtained despite fairly low absorptance (~20%) and moderate η_{PL} (~40%), suggesting ample room for improvement in $\eta_{s,ext}$, by increasing $\eta_{s,abs}$ and/or η_{PL}.

Recently, we reported a new type of CIS QD overcoated with an especially thick ZnS shell, which showed a considerable enhancement in η_{PL} over conventional thin-shell structures, as well as suppressed single-dot PL intermittency and greatly improved photostability[39]. Here, we extend this thick-shell strategy to CISe QDs, which are more suitable for LSC applications due to their narrower bandgap.

We first synthesized CISe cores with an apex to apex size of 3.1 ± 0.5 nm, and then coated them with a thick ZnS layer, increasing the overall particle size to 7.9 ± 0.9 nm (Supplementary Fig. 1; see Methods for details of the synthesis). The PL of these QDs is centred at ~805 nm (Fig. 1b, bottom) and it shows a large width of ~305 meV (full-width at half-maximum, FWHM) typical of these materials[40]. As in the case of CIS QDs, the addition of the thick ZnS shell eliminates fast surface trapping channels (see PL dynamics in Supplementary Fig. 2) and leads to a high η_{PL} of 65–75%, maintained upon matrix encapsulation. This is almost a twofold improvement over the CISeS QDs used in the high-performance LSCs in ref. [7] and ~20% higher than the best literature value for CISe-based QDs[41]. As commonly observed for CISeS QD samples, the absorption spectrum is featureless and exhibits a gradual growth with increasing photon energy after the onset at ~730 nm (Fig. 1b, bottom). This is ~160 meV higher than the PL peak, which helps alleviate the problem of reabsorption.

To fabricate LSCs, we deposited a mixture of CISe/ZnS QDs and polyvinylpyrrolidone (PVP) in chloroform onto 1.59-mm-thick borosilicate glass substrates using a doctor-blade technique[6] (see Methods). The thickness of the QD/polymer film upon drying was 0.05 mm. Figure 2b presents a photograph of a 15.24 × 15.24 cm^2 (~232 cm^2) CISe/ZnS QD LSC with total sunlight absorptance $\eta_{s,abs}$ of 28%. The corresponding visible transmittance (*VT*) is 23%

© 2018 Macmillan Publishers Limited, part of Springer Nature. All rights reserved.

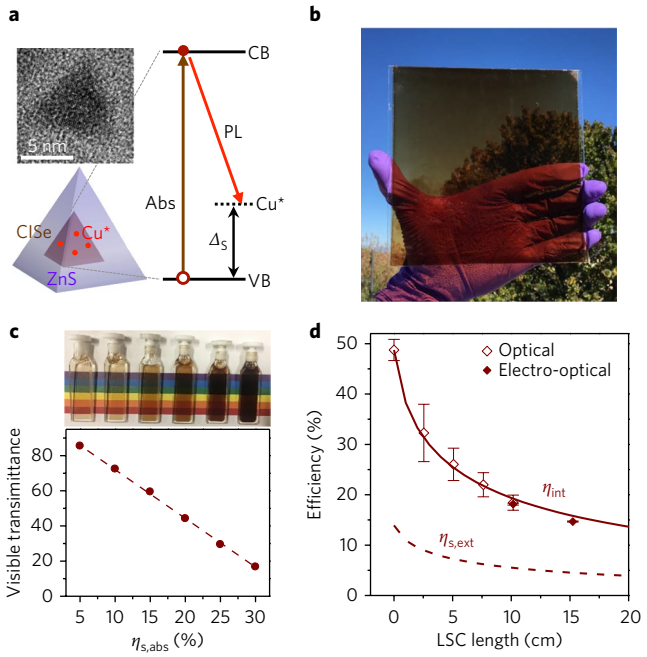

Fig. 2 | Characterization of the bottom tandem-LSC layer based on $CuInSe_2$/ZnS (CISe/ZnS) QDs. a, Top left, Representative TEM image of an individual CISe/ZnS QD schematically depicted at bottom left. Right, Simplified representation of electronic states and optical transitions responsible for light absorption (brown arrow) and PL (red arrow). VB and CB denote valence and conduction bands, respectively; Cu* is a copper-related defect. **b**, Photograph of a large-area (~232 cm^2) CISe-QD LSC. **c**, Top, Solution samples of CISe/ZnS QDs with different sunlight absorptances ($\eta_{s,abs}$) from 5 to 30% (left to right) that correspond to visible transmittances from 85.5 to 16.8%, respectively (bottom). **d**, Length-dependent η_{int} measured by the integrating-sphere (open brown diamonds) and PV (solid brown diamonds) methods. The brown solid line represents modelling. The EQE for sunlight illumination ($\eta_{s,ext}$, brown dashed line) is obtained by multiplying η_{int} by $\eta_{s,abs}$ (=28%).

(Fig. 2c and Supplementary Note 3), so the device appears dark to an observer (Fig. 2b). However, it is still semitransparent and non-hazy, indicating the absence of QD aggregation or other non-uniformities in the polymer matrix, which explains the negligible optical scattering (Supplementary Fig. 3).

We measured the $\eta_{s,ext}$ of square-shaped CISe-QD LSCs as a function of their size (L) by two quantitative techniques, one based on integrating-sphere PL measurements and the other on evaluation of the photocurrent of a PV cell recorded with and without an LSC light collector. The first method provides detailed insights into the optical loss mechanisms by allowing us to differentiate between the numbers of photons emitted from the faces versus the edges of the device[3,6,23] (Supplementary Fig. 4 and Supplementary Note 1). The second method is more relevant to real-life applications as it permits us to directly evaluate the LSC efficiency in terms of the optical-to-electrical PCE[3,8,14,42] (Supplementary Note 2 and Supplementary Fig. 5), and, importantly, it allows for direct measurements under natural sunlight illumination.

Figure 2d presents integrating-sphere measurements of the LSC's internal quantum efficiency as a function of L from 0 to 10.16 cm (open diamonds) for devices with the same $\eta_{s,abs}$ (28%) and η_{PL} (65%). The observed dependence can be accurately described by the analytical model of ref. [19], assuming that propagation losses are dominated by reabsorption, and that losses due to scattering are negligibly small (solid line in Fig. 2d; Supplementary Note 1). The performance of LSCs with L = 10.16 and 15.24 cm was also evaluated using electro-optical measurements (solid diamonds in Fig. 2d). The obtained values are systematically lower than those from optical measurements by ~8 relative percent due to imperfect (92% efficient) coupling of edge-emitted light into the PVs. The L-dependent values of $\eta_{s,ext}$ were obtained by multiplying η_{int} by $\eta_{s,abs}$ (28%): $\eta_{s,ext} = \eta_{int}\eta_{s,abs}$ (Fig. 2d, dashed line). Notably, the performance of our devices is a considerable improvement over the best published results. For example, the value of $\eta_{s,ext}$ = 5.1% measured here for the 12 × 12 cm^2 LSC is ~40% higher than the highest literature value (3.7%) for similarly sized CISeS-QD-based devices[7].

As pointed out previously[7], in addition to demonstrating high EQEs, CISeS-QD-based LSCs are particularly well suited for applications as solar windows as they behave as neutral-density filters that do not introduce significant distortions to perceived colours. At the same time, they allow one to easily control a degree of shading by simply changing the concentration of the QDs (see analysis of VT versus $\eta_{s,abs}$ in Fig. 2c).

Top LSC layer

Next, we demonstrate that a further boost in $\eta_{s,ext}$ is possible by applying a tandem configuration, where the CISe/ZnS-QD LSC is supplemented by a top layer based on Mn^{2+}-doped $Cd_xZn_{1-x}S$ QDs, which increases η_{int} for higher-energy solar photons. As shown previously[22], Mn^{2+}-doped II–VI QDs allow for the realization of low-loss LSCs due to the fact that the d–d emission of the Mn^{2+} ion occurs in a virtually reabsorption-free intragap region of a host semiconductor (Fig. 3a). The most commonly studied Mn^{2+}-doped QDs are based on wide-gap ZnSe and ZnS[22,43]. However, they exhibit only a moderate η_{PL} of up to ~50%[22,43]. A more recent class of Mn^{2+}-doped nanostructures are the Mn^{2+}:$Cd_xZn_{1-x}S$/ZnS core–shell QDs, which can be fabricated using an easily scalable, non-injection method[44]. The use of an alloyed $Cd_xZn_{1-x}S$ core allows for a greater flexibility in controlling the absorption onset and also helps mitigate lattice mismatch with the ZnS shell, leading to high η_{PL} of >70%[44].

For the present studies we synthesized Mn^{2+}-doped $Cd_xZn_{1-x}S$ (x = 0.5) cores with a diameter of 3.0 ± 0.4 nm and then coated them with ~0.7-nm-thick shells (Supplementary Fig. 6). The fabricated structures exhibit a high η_{PL} of 78 ± 2% due to successful suppression of surface-related relaxation by the ZnS shell, as inferred from the measured PL dynamics (Supplementary Fig. 7). The PL peak is centred at ~600 nm, which is ~750 meV below the absorption onset at ~440 nm (Fig. 1b, top). Due to this large spectral shift, the entire PL spectrum resides in the reabsorption-free region, a key to obtaining high η_{int}.

An example of a 20.32 × 20.32 cm^2 (~413 cm^2) LSC fabricated using Mn^{2+}-doped QDs by the doctor-blade method is shown in Fig. 3b. The device absorptance for incident sunlight is fairly small ($\eta_{s,abs}$ = 3.2%), which leads to its colourless appearance (Fig. 3b and Supplementary Fig. 8).

Figure 3c shows η_{int} for a series of LSCs of different dimensions (L = 2.54–20.32 cm) obtained using both optical and electro-optical methods (Supplementary Figs. 9 and 10). The measured η_{int} shows only a small decline with increasing L (symbols in Fig. 3c), which occurs without distortion in the PL spectrum (Supplementary Fig. 8). This indicates that the observed PL loss is not due to reabsorption as in the case of CISe QDs, but weak spectrally independent scattering in the LSC waveguide, which can be modelled using the scattering coefficient of 0.012 cm^{-1} (solid line in Fig. 3c; Supplementary Note 1). Interestingly, the obtained values of η_{int} (>50% even for large, 30 cm device lengths) are close to the reabsorption- and scattering-free limit defined by the product of the light-trapping coefficient for the glass waveguide (η_{trap} of ~75%) and η_{PL}, which yields ~58%.

Because of their low absorptance, the EQEs of the Mn^{2+}-doped-QD devices are in the sub-2% range (dashed line in Fig. 3c).

© 2018 Macmillan Publishers Limited, part of Springer Nature. All rights reserved.

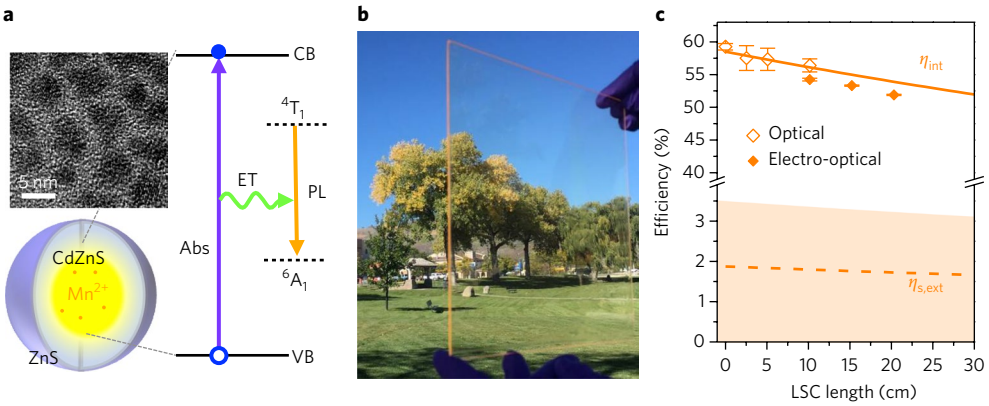

Fig. 3 | Characterization of the top tandem-LSC layer based on Mn^{2+}-doped $Cd_xZn_{1-x}S$/ZnS (CdZnS/ZnS) QDs. a, Top left, Representative TEM image of Mn^{2+}-doped QDs schematically depicted at bottom left. Right, Schematic representation of electronic states and optical transitions responsible for light absorption (purple arrow) and PL (orange arrow). Emission due to the $^4T_1$-to-$^6A_1$ transition of the Mn^{2+} ion is activated by the Auger-type energy transfer (ET, wavy green arrow) from the semiconductor host. **b**, Photograph of a large-area (~413 cm^2) LSC based on Mn^{2+}-doped QDs. **c**, Length-dependent η_{int} measured by optical (open orange diamonds) and PV (solid orange diamonds) methods. The orange solid line represents modelling. Values of $\eta_{s,ext}$ (orange dashed line) are obtained by multiplying η_{int} by $\eta_{s,abs}$ (=3.2%). Orange shading shows $\eta_{s,ext}$ achievable with the saturated value of $\eta_{s,abs}$ of 6%. Note the break in the vertical axis between ~4% and ~40%.

However, by increasing the QD concentration in the polymer matrix, $\eta_{s,abs}$ can be pushed to ~6% (Supplementary Fig. 11). For the 12 cm device this would result in $\eta_{s,ext}=3.4\%$, which approaches the previously reported value of 3.7% achieved with NIR CISeS QDs[7].

Due to their moderate performance when evaluated in terms of $\eta_{s,ext}$, Mn^{2+}-doped-QD LSCs have been primarily considered as model devices well suited for fundamental studies of luminescent concentration in the ideal, reabsorption-free regime, but not real-life applications. Contrary to this common perception, in the next section we demonstrate that Mn^{2+}-doped QDs can enable highly efficient tandem devices when they are combined with CISe-based QDs. Although the latter structures exhibit much stronger overall absorptivity across the solar spectrum, they suffer from incomplete elimination of reabsorption due to the still existing overlap between absorption and emission spectra. By splitting off the higher-energy portion of the solar spectrum with the top layer made of Mn^{2+}-doped II-VI QDs, it is possible to partially mitigate this problem and increase the overall device efficiency.

Tandem LSC design and characterization

A 15.24×15.24 cm^2 (~232 cm^2) prototype tandem LSC based on Mn^{2+}-doped QDs (top layer, $\eta_{PL}=78\%$, $\eta_{s,abs}=4.6\%$) and CISe QDs (bottom layer, $\eta_{PL}=72\%$, $\eta_{s,abs}=24\%$) is presented in Fig. 4a. Due to spectral filtering by the top layer, $\eta_{s,abs}$ of the CISe-QD LSC is reduced from 24% to 17.3%. The absorption onset of the CISe QDs is slightly blueshifted from that of the sample discussed earlier to obtain a better spectral match to the GaAs solar cells used in the complete LSC-PV devices (Supplementary Fig. 12). If the top and the bottom layers are used separately, their EQEs are 2.6% and 5.3%, respectively. In the stacked tandem configuration $\eta_{s,ext}$ increases to 6.4%, which is a ~21% improvement over the single-layer CISe-QD-based device.

To evaluate the tandem LSC performance in a real-life device setting, we conducted measurements of solar-to-electrical PCE using edge-coupled high-efficiency GaAs solar cells (Fig. 4b; see Methods for details). For the coupled LSC-PV system, the current density is calculated from the area of the edge-coupled PVs, while the PCE is obtained based on the solar flux incident onto the LSC. Therefore, although the LSC-PV system can show a higher current density than the standalone PV (due to the effect of concentration), it can still exhibit a lower PCE; this situation is realized with our devices.

According to Fig. 4b, the PCE of a standalone PV (η_{PV}) is 23.7%. The PCE of the coupled LSC-PV system ($\eta_{LSC\text{-}PV}$) can be related to η_{PV} by $\eta_{LSC\text{-}PV}=q\eta_{s,ext}\eta_{PV}$, where q is the spectral reshaping factor calculated as the ratio of the solar-cell EQE averaged over the PL spectrum of the LSC fluorophore and the EQE averaged over the solar spectrum[6] (Supplementary Note 2). Based on the optical performance of our tandem LSC and using $q=2.36$ and 2.12 for the top- and bottom-layer QDs, respectively (Supplementary Fig. 12), we calculated that the PCE of the tandem LSC-PV system should be ~3.4% for the standard AM 1.5G solar spectrum. According to the actual measurements, the top and bottom layers deliver PCEs of 1.3% and 1.8%, respectively (Fig. 4b). This corresponds to a total PCE of 3.1%, which matches exactly the calculations if we account for the 92% LSC-to-PV coupling efficiency, as discussed earlier. Based on these measurements, the tandem configuration allows for ~27% PCE boost, even when using the same types of PV for both LSC layers.

As discussed in Supplementary Note 4, the performance of our tandem devices compares favourably to that of the best reported LSCs based on both QDs and dye molecules[45–48] (Supplementary Tables 1 and 2 and Supplementary Fig. 13). Furthermore, accelerated aging tests of fabricated structures (see Methods) indicate good photostability of both the top and bottom layers (upon proper encapsulation), which should allow for virtually degradation-free operation under standard outdoor conditions for ~9.4 and ~38 months for the CISe-QD and Mn^{2+}-doped-QD layers, respectively (Supplementary Figs. 14 and 15).

To take a full advantage of the tandem geometry, each LSC layer should be coupled to a bandgap-matched PV. In our case, the top Mn^{2+}-doped QD-based LSC layer can, for example, be paired with GaInP PVs (~1.8 eV bandgap). With $\eta_{PV}=20.8\%$ (ref. [49]), the top layer would produce a PCE of 2.0% (assuming again the 8% coupling loss). Combined with the 1.8% PCE of the bottom layer, this will result in a total PCE of 3.8%, which represents a 52% improvement over the single-layer CISe-QD LSC. Even stronger relative enhancement is expected in larger devices, as the beneficial effect of the top layer with higher η_{int} increases progressively with increasing L (compare Figs. 2d and 3c). For example, if we expand the device size to 50 cm, the single-layer CISe-QD LSC coupled to GaAs PVs would deliver a PCE of 1.3%, while the tandem device would more than double this value (PCE of 2.9%) in the case of bandgap-matched PVs.

© 2018 Macmillan Publishers Limited, part of Springer Nature. All rights reserved.

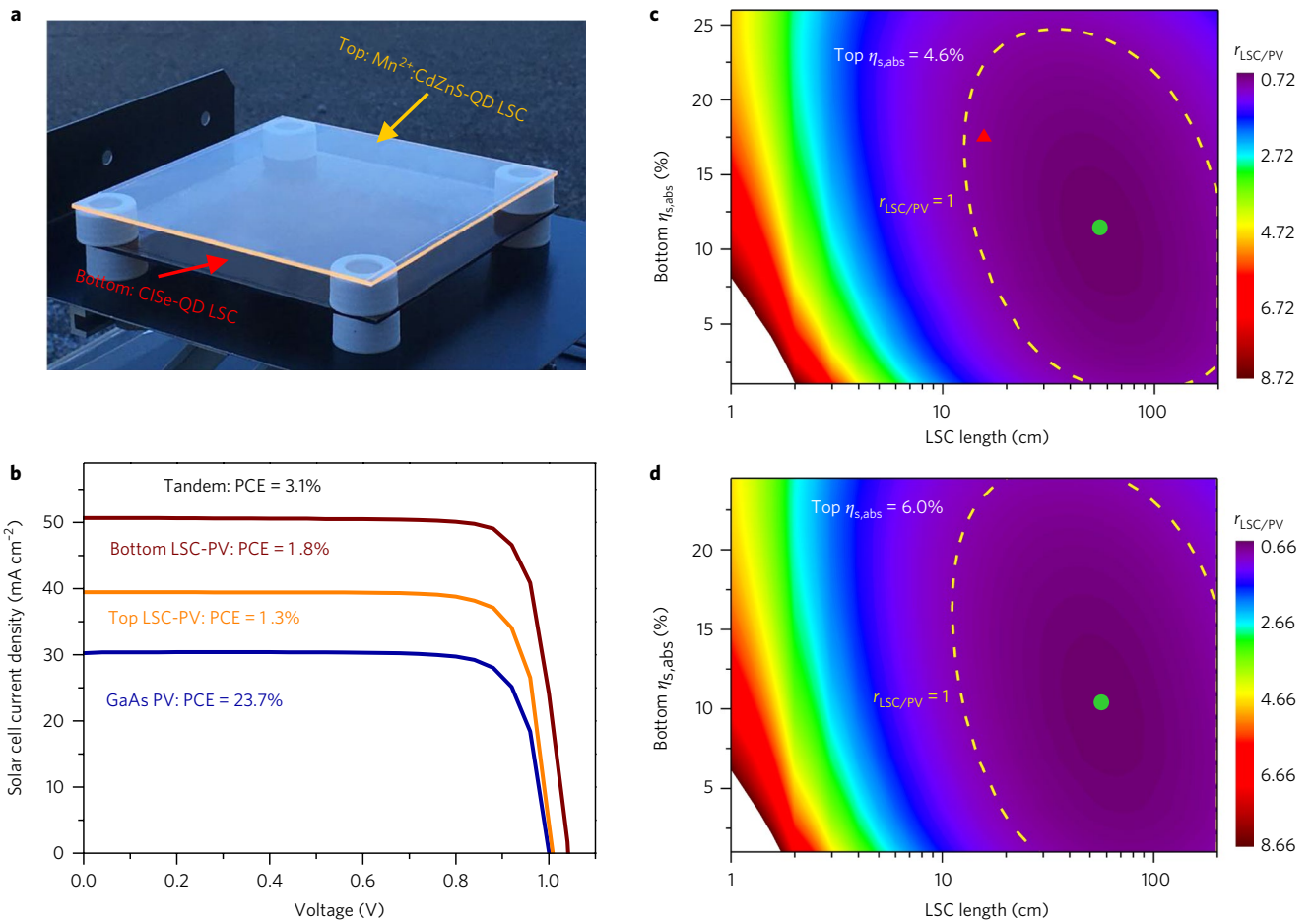

Fig. 4 | A tandem LSC made of the Mn^{2+}:CdZnS-QD top layer and the CISe-QD bottom layer. a, The ~232 cm^2 tandem LSC with the ~2 cm air gap. **b**, Current density versus voltage characteristics of a standalone GaAs PV (blue) and the same type of PVs attached to either the top (orange) or the bottom (brown) LSC layer; natural outdoor illumination with incident power of 104 mW cm^{-2}. **c**,**d**, LSC cost-efficiency factor ($r_{LSC/PV}$) versus bottom-layer absorptance and the LSC length for the fixed absorptances of the top layer of 4.6% (**c**) and 6.0% (**d**). The yellow dashed line ($r_{LSC/PV}=1$) circles the region where an LSC-PV system is more cost efficient than a standalone PV. The red triangle in **c** corresponds to the present tandem ($r_{LSC/PV}=0.87$). Green circles mark the global minima that correspond to $r_{LSC/PV}=0.72$ and 0.66 for $\eta_{s,abs}=4.6\%$ and 6% (**c** and **d**, respectively).

As we discussed in the introduction, one of the motivations for the development of the LSC-PV technology has been a potential reduction in the cost of solar electricity. To evaluate the cost–effectiveness of the developed QD LSC, we performed a comparison of the per watt cost of solar electricity between the standalone Si-PV and the coupled LSC-PV system, which we characterize in terms of the LSC cost–efficiency factor $r_{LSC/PV}$ (Supplementary Note 5 and Supplementary Figs. 16 and 17). Based on our analysis, the cost–efficiency factor for our tandem LSC is 0.87 (red triangle in Fig. 4c), indicating that the LSC-PV system utilizing our devices can in principle be more cost–efficient (by ~13%) than existing Si PV-modules. By further optimizing the LSC dimensions and $\eta_{s,abs}$ of the bottom layer, the cost saving can be increased to ~28% ($r_{LSC/PV}=0.72$; green circle in Fig. 4c). If we increase $\eta_{s,abs}$ of the top layer LSC from 4.6% (used in current devices) to 6.0% (the maximum value achievable with our Mn^{2+}-doped QDs), the maximum attainable cost saving can be boosted to ~34% ($r_{LSC/PV}=0.66$; green circle in Fig. 4d).

In conclusion, we have demonstrated a large-area, high-performance tandem QD-LSC. We have shown that even with a weakly absorbing top layer it is possible to obtain an appreciable improvement in LSC performance if the top-layer internal quantum efficiency exceeds that of the strongly absorbing bottom layer. In the developed prototype 15.24 × 15.24 cm^2 tandems, the PCE improvement versus single-layer devices can exceed 50% (with bandgap-matched PVs) and becomes as large as >120% in devices with a window size of 50 × 50 cm^2. Due to the strong performance achievable with low-cost, solution-processable materials, QD-based tandems and more complex multilayered LSCs can provide a viable pathway to further reduce the cost of solar electricity by complementing the existing PV technology with high-efficiency sunlight collectors deployable either as standalone LSC-PV modules or as semitransparent building-integrated solar windows.

Methods

Methods, including statements of data availability and any associated accession codes and references, are available at https://doi.org/10.1038/s41566-017-0070-7.

Received: 10 July 2017; Accepted: 20 November 2017;
Published online: 01 January 2018

References

1. Weber, W. & Lambe, J. Luminescent greenhouse collector for solar radiation. *Appl. Opt.* **15**, 2299–2300 (1976).
2. Batchelder, J. S., Zewail, A. H. & Cole, T. Luminescent solar concentrators. 1. Theory of operation and techniques for performance evaluation. *Appl. Opt.* **18**, 3090–3110 (1979).

© 2018 Macmillan Publishers Limited, part of Springer Nature. All rights reserved.

3. Currie, M. J., Mapel, J. K., Heidel, T. D., Goffri, S. & Baldo, M. A. High-efficiency organic solar concentrators for photovoltaics. *Science* **321**, 226–228 (2008).
4. Debije, M. G. & Verbunt, P. P. C. Thirty years of luminescent solar concentrator research: solar energy for the built environment. *Adv. Energ. Mater.* **2**, 12–35 (2012).
5. van Sark, W. G. J. H. M. et al. Luminescent solar concentrators—a review of recent results. *Opt. Express* **16**, 21773–21792 (2008).
6. Li, H., Wu, K., Lim, J., Song, H.-J. & Klimov, V. I. Doctor-blade deposition of quantum dots onto standard window glass for low-loss large-area luminescent solar concentrators. *Nat. Energy* **1**, 16157 (2016).
7. Meinardi, F. et al. Highly efficient large-area colourless luminescent solar concentrators using heavy-metal-free colloidal quantum dots. *Nat. Nanotech.* **10**, 878–885 (2015).
8. Zhao, Y. & Lunt, R. R. Transparent luminescent solar concentrators for large-area solar windows enabled by massive Stokes-shift nanocluster phosphors. *Adv. Energ. Mater.* **3**, 1143–1148 (2013).
9. Sholin, V., Olson, J. D. & Carter, S. A. Semiconducting polymers and quantum dots in luminescent solar concentrators for solar energy harvesting. *J. Appl. Phys.* **101**, 123114 (2007).
10. Vossen, F. M., Aarts, M. P. J. & Debije, M. G. Visual performance of red luminescent solar concentrating windows in an office environment. *Energy Build.* **113**, 123–132 (2016).
11. Pritchard, J., Simon, K., Dowd, C. & Joshi, E. Solar power concentrators for space applications. *PAM Rev. Energy Sci. Tech.* **3**, 2–26 (2016).
12. Cambié, D., Zhao, F., Hessel, V., Debije, M. G. & Noël, T. A leaf-inspired luminescent solar concentrator for energy-efficient continuous-flow photochemistry. *Angew. Chem. Int. Ed.* **56**, 1050–1054 (2017).
13. Wilson, L. R., Klampaftis, E. & Richards, B. S. Enhancement of power output from a large-area luminescent solar concentrator with 4.8× concentration via solar cell current matching. *IEEE J. Photovolt.* **7**, 802–809 (2017).
14. Zhao, Y., Meek, G. A., Levine, B. G. & Lunt, R. R. Near-infrared harvesting transparent luminescent solar concentrators. *Adv. Opt. Mater.* **2**, 606–611 (2014).
15. Gutierrez, G. D., Coropceanu, I., Bawendi, M. G. & Swager, T. M. A low reabsorbing luminescent solar concentrator employing π-conjugated polymers. *Adv. Mater.* **28**, 497–501 (2016).
16. Nikolaidou, K. et al. Hybrid perovskite thin films as highly efficient luminescent solar concentrators. *Adv. Opt. Mater.* **4**, 2126–2132 (2016).
17. Zhao, H., Zhou, Y., Benetti, D., Ma, D. & Rosei, F. Perovskite quantum dots integrated in large-area luminescent solar concentrators. *Nano Energy* **37**, 214–223 (2017).
18. Pietryga, J. M. et al. Spectroscopic and device aspects of nanocrystal quantum dots. *Chem. Rev.* **116**, 10513–10622 (2016).
19. Klimov, V. I., Baker, T. A., Lim, J., Velizhanin, K. A. & McDaniel, H. Quality factor of luminescent solar concentrators and practical concentration limits attainable with semiconductor quantum dots. *ACS Photon.* **3**, 1138–1148 (2016).
20. Li, C. et al. Large Stokes shift and high efficiency luminescent solar concentrator incorporated with $CuInS_2$/ZnS quantum dots. *Sci. Rep.* **5**, 17777 (2015).
21. Bronstein, N. D. et al. Quantum dot luminescent concentrator cavity exhibiting 30-fold concentration. *ACS Photon.* **2**, 1576–1583 (2015).
22. Erickson, C. S. et al. Zero-reabsorption doped-nanocrystal luminescent solar concentrators. *ACS Nano* **8**, 3461–3467 (2014).
23. Coropceanu, I. & Bawendi, M. G. Core/shell quantum dot based luminescent solar concentrators with reduced reabsorption and enhanced efficiency. *Nano Lett.* **14**, 4097–4101 (2014).
24. Krumer, Z. et al. Tackling self-absorption in luminescent solar concentrators with type-II colloidal quantum dots. *Sol. Energy Mater. Sol. Cells* **111**, 57–65 (2013).
25. Bradshaw, L. R., Knowles, K. E., McDowall, S. & Gamelin, D. R. Nanocrystals for luminescent solar concentrators. *Nano Lett.* **15**, 1315–1323 (2015).
26. Meinardi, F. et al. Large-area luminescent solar concentrators based on 'Stokes-shift-engineered' nanocrystals in a mass-polymerized PMMA matrix. *Nat. Photon.* **8**, 392–399 (2014).
27. Zhou, Y. et al. Near infrared, highly efficient luminescent solar concentrators. *Adv. Energ. Mater.* **6**, 1501913 (2016).
28. Meinardi, F. et al. Highly efficient luminescent solar concentrators based on earth-abundant indirect-bandgap silicon quantum dots. *Nat. Photon.* **11**, 177–185 (2017).
29. Knowles, K. E., Kilburn, T. B., Alzate, D. G., McDowall, S. & Gamelin, D. R. Bright $CuInS_2$/CdS nanocrystal phosphors for high-gain full-spectrum luminescent solar concentrators. *Chem. Commun.* **51**, 9129–9132 (2015).
30. Tummeltshammer, C. et al. On the ability of Förster resonance energy transfer to enhance luminescent solar concentrator efficiency. *Nano Energy* **32**, 263–270 (2017).
31. Santra, P. K. & Kamat, P. V. Tandem-layered quantum dot solar cells: tuning the photovoltaic response with luminescent ternary cadmium chalcogenides. *J. Am. Chem. Soc.* **135**, 877–885 (2013).
32. Takamoto, T., Ikeda, E., Kurita, H. & Ohmori, M. Over 30% efficient InGaP/GaAs tandem solar cells. *Appl. Phys. Lett.* **70**, 381–383 (1997).
33. Vos, A. D. Detailed balance limit of the efficiency of tandem solar cells. *J. Phys. D* **13**, 839 (1980).
34. Chatten, A. J., Barnham, K. W. J., Buxton, B. F., Ekins-Daukes, N. J. & Malik, M. A. A new approach to modelling quantum dot concentrators. *Sol. Energy Mater. Sol. Cells* **75**, 363–371 (2003).
35. Goetzberger, A. & Greube, W. Solar energy conversion with fluorescent collectors. *Appl. Phys.* **14**, 123–139 (1977).
36. Rice, W. D., McDaniel, H., Klimov, V. I. & Crooker, S. A. Magneto-optical properties of $CuInS_2$ nanocrystals. *J. Phys. Chem. Lett.* **5**, 4105–4109 (2014).
37. Knowles, K. E., Nelson, H. D., Kilburn, T. B. & Gamelin, D. R. Singlet–triplet splittings in the luminescent excited states of colloidal Cu^+:CdSe, Cu^+:InP, and $CuInS_2$ nanocrystals: charge-transfer configurations and self-trapped excitons. *J. Am. Chem. Soc.* **137**, 13138–13147 (2015).
38. Rurack, K. & Spieles, M. Fluorescence quantum yields of a series of red and near-infrared dyes emitting at 600−1000 nm. *Anal. Chem.* **83**, 1232–1242 (2011).
39. Zang, H. et al. Thick-shell $CuInS_2$/ZnS quantum dots with suppressed 'blinking' and narrow single-particle emission line widths. *Nano Lett.* **17**, 1787–1795 (2017).
40. McDaniel, H. et al. Simple yet versatile synthesis of $CuInSe_xS_{2-x}$ quantum dots for sunlight harvesting. *J. Phys. Chem. C* **118**, 16987–16994 (2014).
41. Yarema, O. et al. Highly luminescent, size- and shape-tunable copper indium selenide based colloidal nanocrystals. *Chem. Mater.* **25**, 3753–3757 (2013).
42. Slooff, L. H. et al. A luminescent solar concentrator with 7.1% power conversion efficiency. *Phys. Status Solidi Rapid Res. Lett.* **2**, 257–259 (2008).
43. Beaulac, R., Archer, P. I. & Gamelin, D. R. Luminescence in colloidal Mn^{2+}-doped semiconductor nanocrystals. *J. Solid State Chem.* **181**, 1582–1589 (2008).
44. Levchuk, I. et al. Industrially scalable and cost-effective Mn^{2+} doped $Zn_xCd_{1-x}S$/ZnS nanocrystals with 70% photoluminescence quantum yield, as efficient down-shifting materials in photovoltaics. *Energy Environ. Sci.* **9**, 1083–1094 (2016).
45. Zhao, H. et al. Absorption enhancement in 'giant' core/alloyed-shell quantum dots for luminescent solar concentrator. *Small* **12**, 5354–5365 (2016).
46. Sumner, R. et al. Analysis of optical losses in high-efficiency $CuInS_2$-based nanocrystal luminescent solar concentrators: balancing absorption versus scattering. *J. Phys. Chem. C* **121**, 3252–3260 (2017).
47. Bomm, J. et al. Fabrication and full characterization of state-of-the-art quantum dot luminescent solar concentrators. *Sol. Energy Mater. Sol. Cells* **95**, 2087–2094 (2011).
48. Goldschmidt, J. C. et al. Increasing the efficiency of fluorescent concentrator systems. *Sol. Energy Mater. Sol. Cells* **93**, 176–182 (2009).
49. Green, M. A., Emery, K., Hishikawa, Y., Warta, W. & Dunlop, E. D. Solar cell efficiency tables (version 42). *Prog. Photovolt. Res. Appl.* **21**, 827–837 (2013).

Acknowledgements

This work was supported by the Centre for Advanced Solar Photophysics (CASP), an Energy Frontier Research Centre funded by the US Department of Energy, Office of Science, Basic Energy Sciences. K.W. is a CASP member supported by a LANL Director's Postdoctoral Fellowship.

Author contributions

K.W. and V.I.K. conceived the idea and designed the experiments. H.L. synthesized $CuInSe_2$/ZnS quantum dots. K.W. synthesized Mn^{2+}-doped CdZnS/ZnS quantum dots. H.L. performed microstructural characterizations and stability measurements of the quantum dots. K.W. fabricated and measured the LSC devices and analysed the data. K.W. and V.I.K. wrote the manuscript.

Competing interests

The authors declare no competing financial interests.

Additional information

Supplementary information is available for this paper at https://doi.org/10.1038/s41566-017-0070-7.

Reprints and permissions information is available at www.nature.com/reprints.

Correspondence and requests for materials should be addressed to V.I.K.

Publisher's note: Springer Nature remains neutral with regard to jurisdictional claims in published maps and institutional affiliations.

© 2018 Macmillan Publishers Limited, part of Springer Nature. All rights reserved.

Methods

Materials. Copper(I) iodide (CuI, 99.5%), indium acetate ($In(Ac)_3$, 99.99%), zinc stearate ($Zn(St)_2$, 90%), zinc acetate dihydrate ($Zn(Ac)_2•2H_2O$, 99.99%), cadmium oxide (CdO, 99.99%), manganese acetate tetrahydrate ($Mn(Ac)_2•4H_2O$, 99.99%), sulfur powder (S, 99.99%), selenium pellets (Se, 99.99%), diphenylphosphine (DPP, 98%), dodecanethiol (DDT, 98%), oleylamine (OAm, 70%, technical grade), oleic acid (OA, 90%), octadecene (ODE, 90%), anhydrous ethanol, chloroform, hexane, toluene and polyvinylpyrrolidone (PVP, average molecular weight 40,000) were purchased from Sigma-Aldrich. All chemicals were used as received without further purification.

Synthesis of $CuInSe_2$/ZnS core–shell QDs. The synthesis of $CuInSe_2$/ZnS (CISe/ZnS) core–shell QDs followed previously published procedures with modifications. We first synthesized CISe core QDs following refs [50] and [51]. Briefly, $In(Ac)_3$ (175 mg, 0.6 mmol), CuI (114 mg, 0.6 mmol), OAm (6 ml) and ODE (6 ml) were loaded into a three-neck flask and heated to 80 °C and degassed for 30 mins. The mixture was then heated and stabilized at 210 °C under nitrogen flow. Next, a Se stock solution, prepared in glovebox by dissolving Se pellets (95 mg, 1.2 mmol) in 3 ml OAm and 0.9 ml DPP, was injected into the above mixture at 210 °C. The reaction was allowed to proceed for 40 min at 210 °C before being quenched by lowering the temperature to 80 °C. This core QD solution was degassed at 80 °C to remove any low-boiling-point species and then reheated to 230 °C for ZnS shell growth. The ZnS shell coating on the CISe core was achieved via successive epitaxy growth[52,53]. A ZnS stock solution was prepared by dissolving $Zn(St)_2$ (6.32 g, 10 mmol) in 20 ml ODE, 10 ml OA and 10 ml DDT at 150 °C for 10 min. This stock solution was degassed at 80 °C for 30 min and kept at 50 °C before being added into the CISe core solution four times with 2 h intervals between each injection (~11 ml). After the last injection, the reaction was kept at 230 °C for 4 h. The as-synthesized CISe/ZnS QDs were washed by repeated precipitation with ethanol and finally dispersed in hexane or chloroform for further characterizations.

Synthesis of Mn^{2+}-doped $Cd_xZn_{1-x}S$/ZnS core–shell QDs. The synthesis followed ref. [44] with slight modifications. Several stock solutions were first prepared and stored in air-tight vials under a nitrogen atmosphere. The 0.1 M Zn stock solution was obtained by dissolving $Zn(OAc)_2•2H_2O$ (0.22 g, 1 mmol) in 0.8 ml OAm and 9.2 ml ODE by heating at 160 °C. The 0.4 M Zn stock solution was made by dissolving $Zn(OAc)_2•2H_2O$ (0.88 g, 4 mmol) in 3 ml OAm and 7 ml ODE at 160 °C. The 0.1 M Cd stock solution was obtained by dissolving CdO (0.128 g, 1 mmol) in 2 ml OA and 8 ml ODE at 160 °C. The 0.01 M Mn stock solution was prepared by dissolving $Mn(OAc)_2•4H_2O$ (0.012 g, 0.05 mmol) in 1 ml OAm and 9 ml ODE at 80 °C. The 0.4 M S stock solution was obtained by dissolving S powder (0.128 g, 4.0 mmol) in 10 ml ODE at 160 °C.

For synthesis of the Mn^{2+}-doped $Cd_xZn_{1-x}S$ core, 5 ml DDT and 10 ml ODE were loaded into a three-neck flask and kept under vacuum at 40 °C for 1 h, which was then cooled to room temperature and purged with nitrogen. A 5 ml volume of the 0.1 M Zn stock solution, 5 ml of the 0.1 M Cd stock solution, 5 ml of the 0.01 M Mn stock solution and 5 ml of the 0.4 M ODE-S solution were added to the flask and heated to 230 °C (heating rate of ~20 °C per min) under nitrogen flux. The mixture was kept at this temperature for 1 min before the ZnS shelling process started. A 15 ml volume of the 0.4 M Zn stock solution was added dropwise into the reaction mixture in six steps (2.5 ml per step) with 10 min intervals between the steps. The reaction was quenched in 10 min after adding the last portion by removing the heating mantle. The as-synthesized Mn^{2+}-doped $Cd_xZn_{1-x}S$/ZnS core–shell QDs were washed by repeated precipitation with ethanol and finally dispersed in chloroform for further characterizations.

Characterization of as-prepared QDs. Samples for transmission electron microscopy (TEM) studies were prepared by dropcasting a diluted dispersion of QDs onto carbon-coated copper grids. TEM images were acquired with a JEOL JEM-2100 microscope operating at 200 kV. The elemental analysis was performed via inductively coupled plasma (ICP) optical emission spectroscopy using an ICAP 6000 spectrometer. ICP samples were prepared by dissolving dried QDs in fresh aqua regia before measurements. According to the ICP measurements, the composition of the $CuInSe_2$ core was $Cu_{1.00}In_{1.06}Se_{2.12}$ and the composition of the Mn^{2+}-doped $Cd_xZn_{1-x}S$ core was $Mn_{0.04}Cd_{0.48}Zn_{0.48}S_{1.00}$.

Fabrication of thin-film CISe- and Mn-QD LSCs. Both types of LSC were fabricated by a doctor-blade deposition method[6]. The QDs dispersed in chloroform were carefully cleaned and filtered through 0.25 µm PTFE syringe filters (Sigma-Aldrich) before mixing them with PVP to form a composite. The concentration of the QDs in the slurry was adjusted to prepare LSCs with the desired optical absorptance. To prepare the CISe LSC with an $\eta_{s,abs}$ of 28%, 220 mg CISe/ZnS QDs, 6 g PVP and 20 ml chloroform were mixed and stirred overnight to form a homogeneous QD/PVP slurry. To prepare the Mn-QD LSC with an $\eta_{s,abs}$ of 3.2%, 70 mg Mn^{2+}-doped QDs, 6 g PVP and 20 ml chloroform were mixed and stirred overnight. The mixtures were centrifuged at 2,500 r.p.m. to remove any bubbles in order to obtain high-quality films.

The QD/PVP mixture was poured onto a borosilicate glass substrate to form a strip in front of a glass rod. The rod was swiftly translated over the substrate, leaving behind a viscous QD/PVP layer, which turned into a highly uniform film after evaporation of chloroform. The glass substrates used in the study had a thickness D of 1/16 inch (or 0.159 cm) and the QD/polymer film thickness d was ~50 µm. The geometric gain factor G of the LSCs was calculated from $G = L/[4(D+d)] \approx L/4D$.

Accelerated photostability tests. For the accelerated stability tests, we dropcasted the above QD/PVP composites onto glass substrates, which then dried quickly in air. To protect the QDs from direct exposure to air and to mimic the QD encapsulation used in, for example, commercial QD-based displays, the films were loaded into customized airtight cuvettes under a nitrogen atmosphere in a glove box. To test photostability, the films were exposed to 462 nm light (for CISe QDs) or 405 nm light (for Mn^{2+}-doped QDs) from blue LEDs (Thorlabs). The power densities incident onto the CISe and Mn^{2+}-doped QD films were 1.57 and 0.75 W cm^{-2}, respectively. Based on the absorption spectra of the films, the corresponding acceleration factors F_A were 56 and 230.

The PL quantum yields of the films were monitored at 12 h intervals, as shown in Supplementary Figs. 14 and 15. According to these measurements, η_{PL} dropped by 3.5 and 5.7% for CISe and Mn^{2+}-doped QD films, respectively, after 48 h of LED illumination, which translates into 0.31 and 1.26 years of continuous exposure to natural sunlight, or 0.78 and 3.18 years in an outdoor environment if one accounts for the day–night cycle (~9.5 h per day on average in New Mexico, USA).

Measurement of LSC performance. The efficiencies of the fabricated LSCs were measured by two different methods: a purely optical method using an integrating sphere[3,6,23] and an electro-optical method by measuring current density versus voltage (J–V) characteristics of PV cells attached to LSC edges[3,8,14,42]. In the integrating-sphere measurement, we used a 'fibre-in–fibre-out' configuration as in ref. [6]. Due to the size limitation of the integrating sphere, the largest LSC size tested by this method was L = 10.24 cm. A 385 nm LED was coupled to the input fibre as the illumination source. The tested LSC (edge-masked or not) was shielded from direct exposure to incident LED light by a baffle. A second baffle was placed in front of the output fibre. The LED light and the light emitted by the LSC were collected by the output fibre and detected by a compact spectrometer (Ocean Optics). The wavelength-dependent detectivity of the system was obtained by measuring the spectrum of a lamp with a certified emission colour of 3,300 K (Ushino FCR 12V100W). The same set-up was used to determine the absolute PL quantum yields (QYs) of QD solution samples.

For J–V measurements on single-junction LSCs, we used polycrystalline silicon (c-Si) solar cells (Solar Made) with an area of 0.5 cm × 2.5 cm. The PV cells were attached to one edge of an LSC using an index-matching polymer adhesive (NOA 68, Norland Products). The width of the PV cell (0.5 cm) was larger than the thickness of the LSC (~0.164 cm), so we used black tape to mark the excess area of the cell. The J–V curves of the coupled LSC-PVs and the standalone PV were obtained using a voltage source meter (Keithley 236) in the range of −0.5 V to 0.7 V with a voltage step of 0.02 V. The J–V curves shown for these single-junction LSC-PVs were all obtained under outdoor conditions on a sunny day with a sunlight power of 88 mW cm^{-2}.

For the J–V curve measurements of the tandem LSC we used thin-film GaAs solar cells (purchased from Alta Devices) with an area of 1.7 cm × 5 cm. The excess areas of the cells were masked by black tape. The J–V curves of the coupled LSC-PVs and the standalone PV were collected using a voltage source meter (Keithley 236) in the range of −0.2 V to 1.2 V with a voltage step of 0.04 V. Measurements were performed in outdoor conditions on a sunny day around noon; the measured sunlight power was 104 mW cm^{-2} and the outdoor temperature was 9–10 °C. The tested device (an LSC or a reference standalone solar cell) was oriented to achieve the maximum short-circuit current; this condition corresponded to normal incidence of direct sunlight onto the device under investigation.

In all LSC-PV measurements (for both single-layer and tandem devices), after attaching solar cells to the LSC the excess edge areas were masked with black strongly absorbing tape.

Data availability. The data that support the plots within this paper and other findings of this study are available from the corresponding author upon reasonable request.

References

50. Panthani, M. G. et al. $CuInSe_2$ quantum dot solar cells with high open-circuit voltage. *J. Phys. Chem. Lett.* **4**, 2030–2034 (2013).
51. Du, J. et al. Zn-Cu-In-Se quantum dot solar cells with a certified power conversion efficiency of 11.6%. *J. Am. Chem. Soc.* **138**, 4201–4209 (2016).
52. Li, L. et al. Efficient synthesis of highly luminescent copper indium sulfide-based core/shell nanocrystals with surprisingly long-lived emission. *J. Am. Chem. Soc.* **133**, 1176–1179 (2011).
53. Zhang, A. et al. Non-blinking (Zn)CuInS/ZnS quantum dots prepared by in situ interfacial alloying approach. *Sci. Rep.* **5**, 15227 (2015).

© 2018 Macmillan Publishers Limited, part of Springer Nature. All rights reserved.